Corrosion Science 199 (2022) 110175

Contents lists available at ScienceDirect

Corrosion Science

journal homepage: www.elsevier.com/locate/corsci

Controllable defect engineering to enhance the corrosion resistance of Cr/GLC multilayered coating for deep-sea applications

Yingrui Liu [a,b,1], Shuyu Li [a,b,1], Hao Li [a,b], Guanshui Ma [a], Lili Sun [a], Peng Guo [a], Peiling Ke [a,b,*], Kwang-Ryeol Lee [c,**], Aiying Wang [a,b,*]

[a] Key Laboratory of Marine Materials and Related Technologies, Zhejiang Key Laboratory of Marine Materials and Protective Technologies, Ningbo Institute of Materials Technology and Engineering, Chinese Academy of Sciences, Ningbo 315201, PR China
[b] Center of Materials Science and Optoelectronics Engineering, University of Chinese Academy of Sciences, Beijing 100049, PR China
[c] Computational Science Center, Korea Institute of Science and Technology, Seoul 136-791, Republic of Korea

ARTICLE INFO

Keywords:
Sputtered films
EIS
Polarization
Pitting corrosion
Anodic dissolution

ABSTRACT

A cleaning intervention is introduced to control the growth defect of Cr/GLC multi-layered coating to avoid premature failure in the deep-sea environment. The results demonstrated that the introduction of the cleaning intervention significantly decreased the penetrating defect density as expected, together without deteriorating the superior mechanical and tribocorrosion properties. The localised corrosion resistance was improved dramatically in the simulated deep-sea environment. It was illustrated that controllable defect engineering can be an effective strategy for improving the anti-tribocorrosion performance of GLC coatings for harsh deep-sea applications.

1. Introduction

Owing to the intense progress in marine exploration and deep-sea development, e.g. submarine natural gas exploitation and submersion of oil pipelines, corrosion and wear now account for the two most critical challenges for moving mechanical components/systems in marine environments [1–4]. High corrosion rate is undesirable because it causes the early degradation of materials and the subsequent failure of components, as well as the damage of systems. Concurrently, material wear is also considered a safety hazard because of the rapid removal of material, as well as the extra energy that must be expended to overcome it, and this causes energy loss [5–7]. Particularly, dissimilar to offshore conditions, the most distinctive feature of a deep-sea environment is the high hydrostatic pressure, which increases by 1 MPa for every 100-m depth [8,9], it can accelerate the failure of marine equipment. Several studies have focused on investigating the corrosion and wear behaviours, such as pitting corrosion [10], galvanic corrosion [11], and tribocorrosion [12] as well as water diffusion in the coatings [13,14], of different materials, including metals and coatings, in deep seas. The results demonstrated that the materials (metals and coatings) suffered from high hydrostatic pressure-induced severe corrosion or wear attacks in the deep sea. This intense progress requires a new strategy (a coating technique) that can ensure extensive anti-corrosion and anti-wear performances for moving mechanical components, such as plungers of seawater pump and water-lubricated bearing, in deep seas [15–17].

Among the wide range of developed protective coatings, graphite-like carbon (GLC) coating is considered a promising candidate for the desired surface coating because of its excellent combination of solid lubrication and chemically inert properties, as well as a specific layered structure [18,19]. Previous reports confirmed that GLC coatings enhanced the tribological and anti-corrosive properties of metallic substrates, which subsequently benefitted the lifetime of working components that were utilised in automotive injection parts, aerospace gears, and fuel cell plates, etc. [20–23]. Furthermore, most corrosion behaviours of GLC coatings exhibit a strong dependence on their compactness, which is closely related to the growth defects that are generated in the coating during the line-of-sight plasma transfer of the physical vapour deposition (PVD) process. Generally, the growth defects of GLC coatings include pinholes, nodules, pores, crevices, and other discontinuities [24]. Upon exposing a substrate to corrosive media, the

* Correspondence to: Ningbo Institute of Materials Technology and Engineering, Chinese Academy of Sciences, Ningbo 315201, PR China.
** Corresponding author.
E-mail addresses: kepl@nimte.ac.cn (P. Ke), krlee@kist.re.kr (K.-R. Lee), aywang@nimte.ac.cn (A. Wang).
[1] These authors contributed equally to this work.

https://doi.org/10.1016/j.corsci.2022.110175
Received 10 October 2021; Received in revised form 1 January 2022; Accepted 12 February 2022
Available online 18 February 2022

corrosive electrolyte would penetrate the substrate through such defects. Anodic dissolution occurs at the exposed points on the substrates [25,26]. Thus, the growth defects that directly expose the substrate are a particularly critical hazard for protective coatings because they account for the starting points of an environmental corrosion attack.

Several methods, such as substrate ion pre-etching, atomic layer deposition (ALD), and multi-layered approaches [24,27–30], have been adopted to reduce the porosity of GLC coatings and improve their corrosion resistance. Among these methods, the multi-layered approach has been demonstrated as an effective strategy for improving corrosion resistance and mechanical properties [31]. Li et al. [32] investigated the relationship between the multilayer structure and tribocorrosion performance of a Cr/GLC coating, the results demonstrated that an ideal multilayer structure of the Cr/GLC coating (1:3) could inhibit defect propagation and protect the substrate. Cui et al. [33] demonstrated that the corrosion resistance of a multilayer amorphous carbon film is much superior compared with those of the substrate and a single layer film. The improved corrosion resistance of the multi-layered structure coating is mainly attributed to the extensive ion diffusion pathway in the coating and the terminated pinholes at the interface of the layers. Thus, the higher the number of interfaces and alternating embedded layers at a given total coating thickness, the better the corrosion resistance [34]. However, the growth defects that completely expose the substrates (designated as penetrating defects) are widespread, which is considered the significant challenges that must be overcome. This type of defect is generally caused by the disintegration of the remaining absorbed particles on the surface of the substrate after the deposition or particles that were generated during the deposition. It is also evident in multi-layered coatings [35,36]. Our previous studies demonstrated that the tribocorrosion performance of a GLC coating at atmospheric pressure is significantly enhanced after using ideal metal buffer layers (Cr doping) for an optimum modulation period [37]. However, the corrosion resistance of this kind of Cr/GLC multi-layered coating decreases significantly, following an immersion test in a deep-sea environment (30 MPa) for 240 h [38]. The detailed analysis performed in this study confirmed that the high hydrostatic pressure of the deep-sea environment enhanced the diffusion of seawater through the penetrating defects and accelerated the localized corrosion of the substrate significantly. Park et al. [39] reported that the penetrating defects significantly affected the tribological behaviour of diamond-like carbon (DLC) films in aqueous environments. By interrupting the DLC deposition process via additional ultrasonic cleaning, they evidently demonstrated the effect of the penetrating defects on the coating failure in an aqueous environment. Thus, controlling the penetrating defects is crucial to high-quality GLC coating in deep-sea environments. To the best of our knowledge, only a few studies have focused on the penetrating defects that are induced in multi-layered coatings.

In this study, we demonstrated that applying the cleaning intervention to the deposition process was a highly effective strategy for decreasing the penetrating defect density in typical Cr/GLC multi-layered coatings, the details of the fabrication process were introduced, and the mechanism of improving the clean intervention was detailedly discussed. Further, a series of electrochemical methods were adopted to investigate the corrosion behaviours under atmospheric and hydrostatic pressure conditions. The cleaning intervention availed a direct and effective method for further enhancing the corrosion resistance of Cr/GLC multi-layered coatings, and this method is greatly significant to deeply understand the formation mechanism of growth defects theoretically for practical applications in deep-sea environments.

2. Experimental process

2.1. Coating deposition

Cr/GLC multi-layered coatings were prepared on mirror-polished 17–4 PH stainless-steel (φ = 17 mm × 3 mm) substrates via direct current magnetron sputtering (DCMS). Before the deposition, the substrates were ultrasonically cleaned in acetone for 20 min, followed by ethanol for 15 min. When the chamber vacuum was lower than 4×10^{-5} Pa , all the substrates were etched and pre-cleaned in Ar^+ for 40 min with a substrate bias of − 200 V. During the deposition, Ar was introduced to sputter the gargets in a flow of 50 sccm. Next, a (Cr + Cr_xN) buffer layer was first deposited with a bias voltage − 100 V, followed by an N_2 flow of 20 sccm for 8 min. The GLC layer was deposited with a graphite target and a bias voltage of − 200 V. The currents of the Cr (dimension = 380 mm × 100 mm × 7 mm, purity = 99.99%) and graphite (dimension = 380 mm × 100 mm × 7 mm, purity = 99.99%) targets were 3.5 and 3.0 A, respectively. The deposition times for the middle Cr, GLC, and top GLC layers were 4, 22, and 50 min, respectively. The Cr/GLC multi-layered coatings were fabricated via the alternative depositions of the Cr and GLC layers. The procedures for depositing the Cr and GLC coats were set to one cycle; eight cycles were repeated to obtain the Cr/GLC multi-layered coating. Fig. 1 show the schematic of the deposition equipment and Cr/GLC multi-layered coating.

Further, a manual cleaning intervention was introduced during the alternative deposition of the Cr/GLC multi-layered coatings to remove the absorbed particles on a certain surface. Specifically, the cleaning process comprised three steps: (1) the ultrasonic washing with alcohol-based cleaning agents for 15 min, (2) the swabbing of the surface with a cotton swab, and (3) drying in high-pressure pure N_2 flow. Different cleaning intervention times were adopted to fabricate three kinds of Cr/GLC multi-layered coatings, as follows: Sample 1 (S1) was fabricated employing the alternative deposition method and without the cleaning intervention, Sample 2 (S2) was fabricated with one cleaning intervention on the surface of the 5th Cr layer, and Sample 3 (S3) was prepared employing two cleaning interventions on the surfaces of the 3rd and 6th Cr layers. The schematic diagrams of the multi-step deposition process protocol can be found in Fig. 2. To avoid the influence of the oxidation film, which was formed during the cleaning intervention, on the adhesion performance, the cleaned Cr layers were etched with Ar^+ for 10 min in the later alternative deposition process to remove the oxide film that formed during the intervention. Accordingly, the deposition time for these Cr layers, which underwent the cleaning intervention, was increased to 5 min to ensure uniform thickness.

2.2. Coating characterisation

The surface and cross-sectional morphologies of the coatings and growth defects were characterised via field-emission scanning electron microscopy (FESEM; FEI, Quanta 250 FEG, USA) with energy-dispersive X-ray (EDX) (Oxford, UK) at voltages of 10 and 15 kV, respectively. The microstructure of the coatings was characterised via high-resolution transmission electron microscopy (HRTEM; FEI, TF20, USA). The formation mechanism of the growth defects was analysed via SEM and focused ion beam (FIB, Carl Zeiss, Auriga, GER) techniques. The acceleration voltage and beam current were 30 kV and 4 nA, respectively. Following the electrochemical tests, the morphologies of the coatings were observed employing an optical microscope (LEICA, M125, GER). The hardness and elastic modulus of the coatings were tested by using a nano-indenter (Nano Indenter, MTS Ltd, USA). To avoid the effect caused by the substrate, the hardness of the coating was selected in the displacement into surface of 180 nm.

2.3. Electrochemical corrosion and tribocorrosion tests

The influence of the cleaning intervention on the corrosion behaviour of the Cr/GLC multi-layered coating was studied via a series of electrochemical methods on a Modulab electrochemical workstation (Solectron Analytical). A three-electrode system comprising Ag/AgCl, a Pt wire, and the samples as the reference, counter, and working electrodes, respectively, was utilised. The corrosion resistance of the

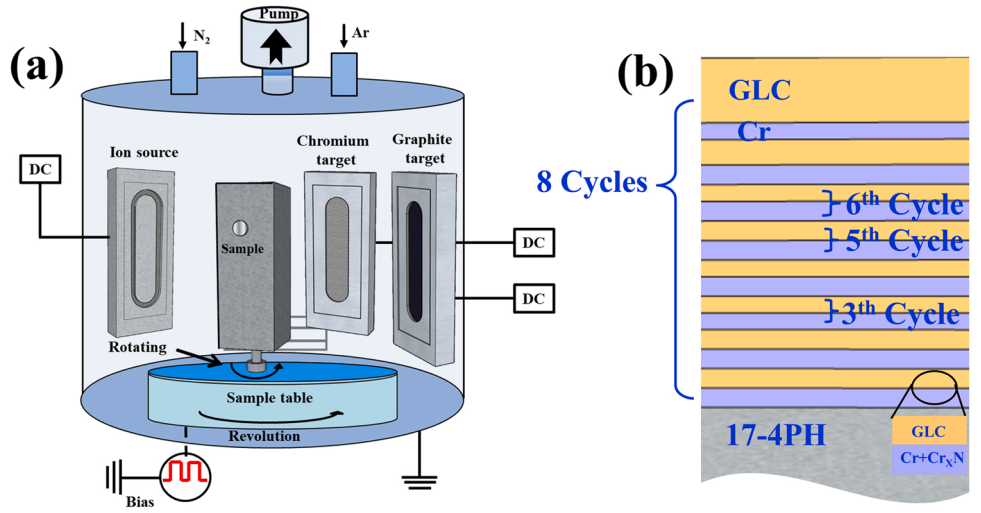

Fig. 1. Schematic of the coating deposition system(a) and schematic of the Cr/GLC multi-layered coating (b).

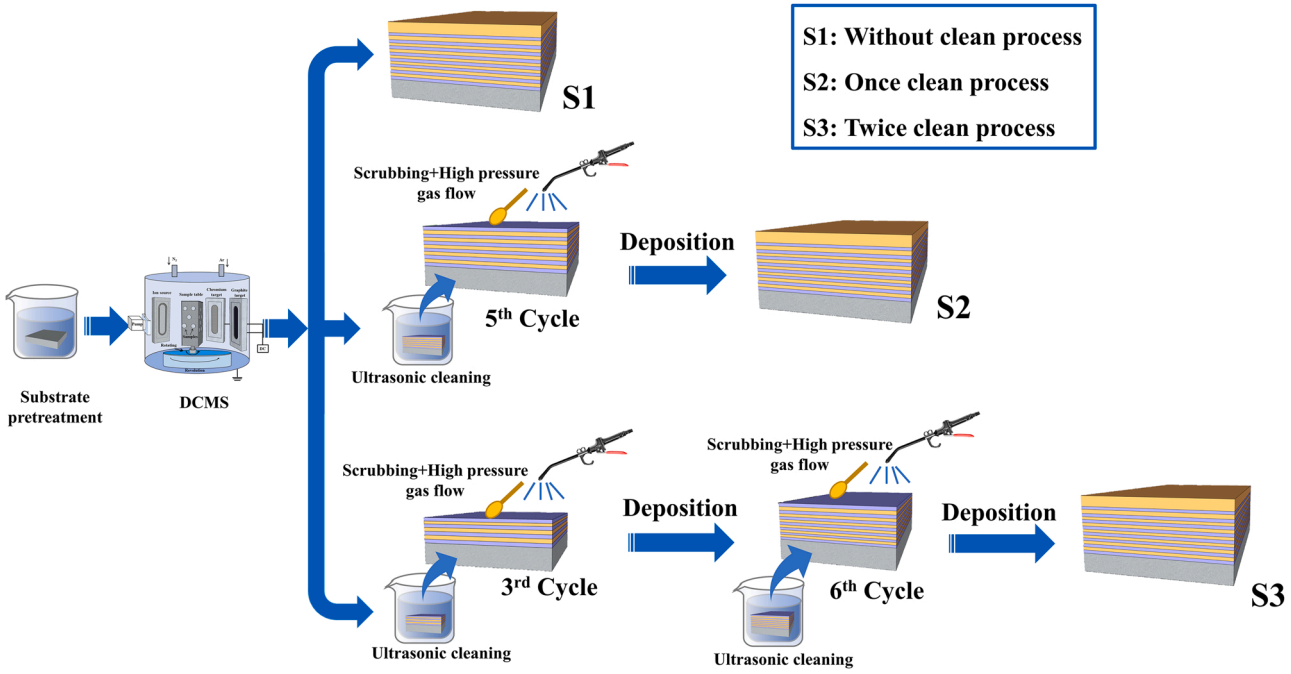

Fig. 2. Schematic diagrams of the multi-step deposition process protocol. Three kinds of Cr/GLC multi-layered coatings (S1-S3) with different number of clean intervention processes were fabricated. S1 sample fabricated with the consecutive deposition process. S2 sample fabricated with one clean process at 5th cycle Cr layer. S3 sample fabricated with two clean processes at 3rd and 6th cycle Cr layers.

coatings was evaluated via electrochemical impedance spectroscopy (EIS) and potentiodynamic polarization tests in a 3.5 wt% NaCl solution. Before the electrochemical experiments, all the samples were immersed for 1 h to stabilise the surface of the coatings. The EIS tests were conducted at a perturbing AC amplitude of 10 mV and scanning frequencies of 10^5-10^{-2} Hz. All the data were analysed and fitted with electrical equivalent-circuit models employing the ZSimpwin software. The potentiodynamic polarization test was scanned from − 0.5 V (below the open-circuit potential (OCP)) to + 1.5 V at a sweep rate of 2 mV/s. The potentiostatic polarization test was measured for 150 min at 0.4 $V_{VS\ OCP}$.

To investigate the corrosion resistance of the different coatings in the deep-sea environment, an immersion test was conducted for 300 h in a simulated deep-sea autoclave corrosion test system at high hydrostatic pressure (31 MPa). The details of the test equipment are presented in our previous report [38]. The samples were immersed in artificial seawater at 10 °C in a high-pressure autoclave. The EIS tests were conducted after the immersion for 300 h at 31 MPa. The test parameters were the same as those utilised in the normal pressure test.

To evaluate the tribocorrosion performance of the different coating samples in 3.5 wt% NaCl solution after conducting the cleaning intervention, tribocorrosion tests were carried out on the liner reciprocating tribometer equipped with a typical three electrode electrochemical system, the detailed information tribocorrosion setup can be found in supporting information S1. All the tribocorrosion tests were conducted at a normal load of 5 N. The sliding velocity and stroke length were set at 0.02 m/s and 5 mm, respectively. The commercial Si_3N_4 balls (Φ 6 mm) was set as the counterpart. The total sliding time was 1 h for all coatings. After the sliding tests, the cross-sectional profiles of the wear tracks were measured by a surface profilometer (Alpha-Step-IQ). The tribocorrosion performance of the different coating samples was evaluated in terms of

calculating the wear rate by using the following equation:

$$W = V/(F \times L) \quad (1)$$

where V is the wear volume loss in mm^3, F is the applied normal load of N and L is the total sliding distance in m[37].

3. Results and discussions

3.1. Cross-sectional morphologies of the coatings

Fig. 3 shows the cross-sectional morphologies of the deposited Cr/GLC multi-layered coatings with different numbers of cleaning interventions. These coatings exhibited a typical multi-layered structure, and the overall thickness was in the range of 1.72–1.96 μm, slightly increasing with the cleaning intervention time. Additionally, the insets in Fig. 3(c) and (d) show the enlarged views of the cleaned Cr layers in S2 and S3, which was thicker compared with the other normal Cr interlayers, and adhered well to the surrounding GLC layers, thus demonstrating that the slight increase in the overall thickness originates from the prolonged deposition time for these cleaned Cr layers. Moreover, all the Cr and GLC layers exhibited fluctuations. Fig. 3(b) presented the HRTEM image of the composite buffer layer and the SEAD results confirmed that buffer layer is Cr+Cr_2N. The Cr and GLC layers were uneven and wavy, and the selected area electron diffraction (SAED) results of the GLC and Cr layers revealed their typical amorphous and nanocrystalline structures, which agree with the results in the reference [32]. The following accounts for the fluctuation of the layers: the first buffer layer in this coating was the (Cr+Cr_2N) composited layer, which generally exhibits typical columnar crystal features; thus, the subsequently deposited layers would completely cover the surface of the columnar crystal. During the deposition process, all the morphological features of the surface of the uneven buffer layer were transferred onto the subsequent layers and even magnified. Growth defects, such as pinholes or coarse columnar grain boundaries, largely exist in single layers, which affects the corrosion resistance of the coating. Consequently, the multi-layered structure availed additional interfaces to prevent the growth of these defects and significantly prolong the diffusion of the corrosive species (Cl, O, etc.) through these micro-pathways.

3.2. Typical growth defects in the Cr/GLC multi-layered coating

Although the multi-layered Cr/GLC coating exerted an excellent shielding or healing effect on micro-defects, such as the pinholes, the catastrophic failure of the coatings and localised corrosion were the most reported consequences of the penetration of an electrolyte through the defects, which exhibited larger scales and directly exposed the substrates. Therefore, the mechanism of the formation of the penetrating defects and its influence on the localised corrosion process must be specially described. Fig. 4 shows the typical surface morphologies and corresponding features of the penetrating defect in S1 without a cleaning intervention during the deposition. As revealed by the low-magnification surface morphologies (Fig. 4(a)), the as-deposited sample was flat and smooth, although several tiny growth defects could be observed. Fig. 4(b) shows the detailed image of the surface characteristics of the defects that were marked at position A, and Fig. 4(c) exhibits its cross-sectional features from position c. Apparently, this defect corresponds to the open type and completely exposed the substrate, indicating that this type of defect would ease the occurrence of a corrosion attack at this weak pit. Fig. 4(d) show other typical defects in S1; they are generally termed nodular-like defects [40]. Nodular-like defects are the most common type of growth defects that accompany PVD coatings. This nodular-like defect in position B was probably caused by a seed (Fig. 4(e)) [41]. This seed typically originates from some particles, such as dust in the air or the particles that were ejected from the coating material sources, or substrate protrusions, such as metallurgical inclusions [42,43]. In this study, the corresponding EDS mapping results (Fig. 4f)) revealed that the seed was a chromium nitride particle, which originated from the Cr target. Since the buffer layer of this Cr/GLC multi-layered coating is a composite layer of Cr+Cr_2N and the Cr_2N layer was fabricated via reactive magnetron sputtering, the introduction of a reactive N_2 gas might cause the poisoning of the Cr target, which would subsequently produces the erupted nitrides from the surface of the poisoned Cr target and act as a seed in the subsequent deposition

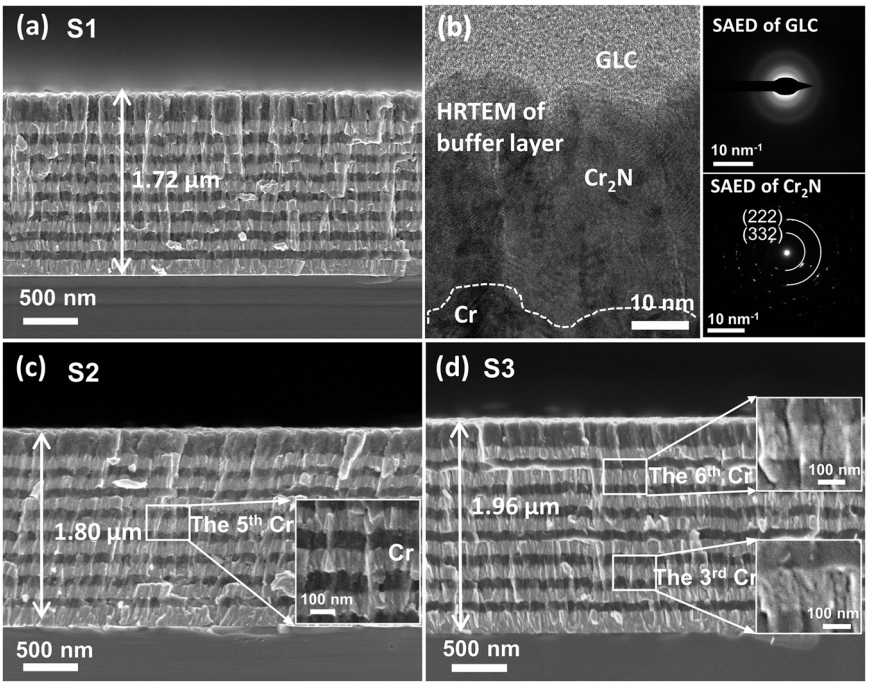

Fig. 3. Cross-sectional images of the as-deposited coatings (a), Detailed HRTEM image of the buffer layer and its corresponding SAED of GLC and Cr2N(b). S2 sample (c) and S3 sample (d).

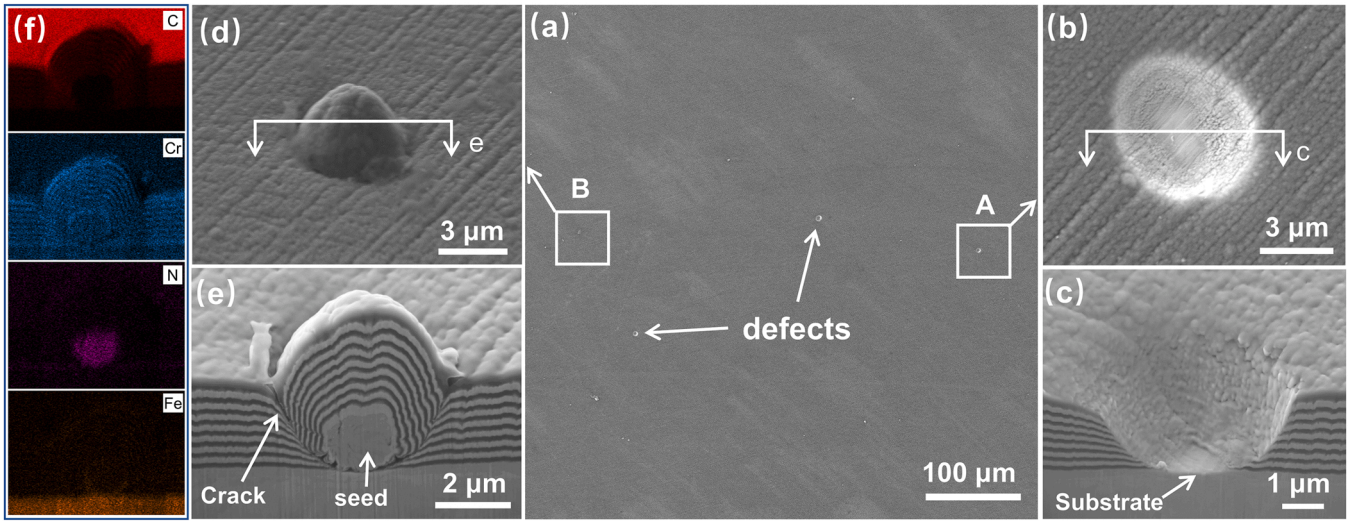

Fig. 4. Surface morphologies and corresponding growth defect characteristics of S1 sample. Surface morphology(a) and enlarged typical penetrating defect and its corresponding cross-sectional image(b)-(c), typical local bulge (d) and corresponding cross-sectional images(e), and the EDS mapping spectrum(f).

process [44]. The nodular-like defect begins to grow in the shape of an inverted cone that propagates through the overall coating before finally forming a domed protrusion at the outer surface. Owing to the shadowing of the vapour flux by the seed particle and the consequent limited thermal mobility of the atoms on the surface[45], significantly discontinuous boundaries (marked as crack in Fig. 4(e)) would exist between the nodule and surrounding coating matrix. This crack represents a region of weakness, and the nodule might be completely detached from the coating surface, leaving the penetrating defect behind.

Another typical open-type defect feature that was induced by the detachment of the nodular-like defects is shown in Fig. 5. These growth defects differed from those displayed in Fig. 4. Fig. 5(b) shows that this defect no longer belonged to the through-thickness defect. The detailed morphological characteristics (Fig. 5(c) and (d)) and corresponding EDS mapping results of the defect at position A (Fig. 5(a)) indicated that it only exposed the Cr interlayer behind. According to the morphological features of the defect in Fig. 5(c), it was referred to as crater-like defects. Fig. 5(e)-(f) show the formation process of such crater-like defects. The seed would be overgrown by the coatings if the micro-particles appear at the interlayer and act as a seed, and the contour of the coating would subsequently follow the shape of the seed. As discussed, owing to the low adhesion strength between the nodular-like defect and the surrounding matrix, some nodular-like defects detached from the coating and leave a crater on the coating surface. Fig. 5(e) shows evidence of typical nodular-like and crater-like defects. Moreover, an irregular carbon particle accounted for the origin of the seed particles in Fig. 5(g) and it differed from the seed in Fig. 4(e). Although the crater-like defect exposed the Cr interlayer, the corrosion protection of this type of defect was better than that of the penetrating defect.

The foregoing analysis indicated that any protrusion on the substrate or interlayer was a seed for the formation of nodular-like defects owing to the wide source of the seeds. Furthermore, the nodular-like defects could be very easily detached from the surface because of the poor adhesion strength at the boundary to eventually cause the most harmful defect (the penetrating defect). Thus, it was practically impossible to eliminate penetrating defects in the Cr/GLC multi-layered coatings during the deposition. Therefore, the introduction of the cleaning intervention to remove the nodular-like defects was a feasible method that would not change the coating structure and deposition parameters. The cleaning intervention reduced the possibility of forming the

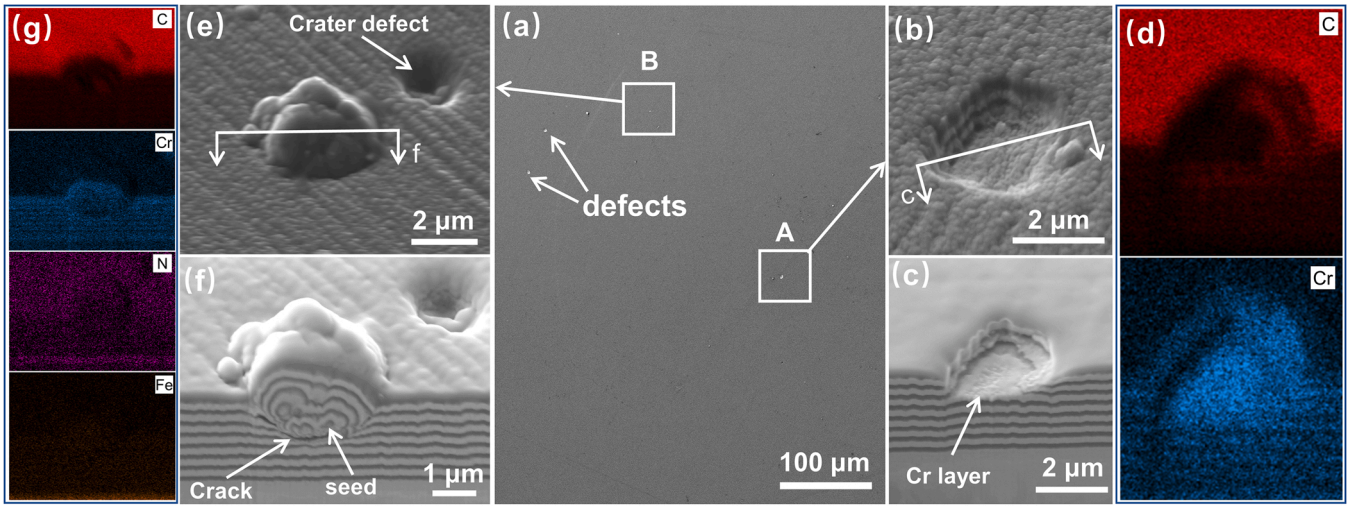

Fig. 5. Surface morphologies and corresponding growth defect characteristics of S2 sample. Surface morphology(a), the enlarged typical penetrating defect and its corresponding cross-sectional image(b) and (c), EDS mapping spectrum(d), typical local bulge (e) and the corresponding cross-sectional image (f), EDS mapping spectrum (g).

penetrating defect, which was significantly harmful to the corrosion resistance.

Fig. 6 shows the surface morphology and the corresponding EDS results of the crater-like defect, which were obtained from the sample that was subjected to two cleaning interventions at the 3rd and 6th Cr interlayers, respectively, during the alternative deposition. Fig. 6(a) shows that the crater-like defect was covered with an irregular coating. The EDS results indicated that this irregular area exerted a good protective effect on the substrate. The mechanism of the formation of the nodular-like defects, as previously analysed, confirmed that this patch-like defect exhibited a typical feature of a healed penetrating defect or a crater-like defect. The introduction of the cleaning intervention during the alternative deposition in this study eased the detachment of the nodular-like defects from the current-cleaning surface. Subsequently, the deposited layers were deposited on the surface of the cleaned Cr interlayers to heal the craters. Regardless of the layer (the substrate, GLC, or Cr layers) that the defect exposed, the subsequent deposition covered the bottom of the defect and eventually sealed these exposed imperfections, thus yielding a denser Cr/GLC multi-layered coating.

The penetrating defects in this multi-layered coating exerted the most significant effect on the corrosion resistance of the coated components. On the one hand, it availed a wide-open pathway for the corrosive species to corrode the substrate. More critically, the catastrophic failure of the coating was induced by the damage of the interface, beginning from these defects. The detachment of the nodular-like defects left an exposed substrate or interlayer; the earlier the nodular was formed, the later it was detached, and the deeper the defect, the worse the sealing effect on these crater-like defects during the subsequent deposition process. Therefore, the defects would be formed during the deposition, following the cleaning intervention, although the possibility that this newly formed defect would align with the existing defect on the surface is extremely low. This is how the cleaning intervention could eventually remove the penetrating defects.

3.3. Mechanical and tribocorrosion properties of the coatings

The mechanical properties of Cr/GLC multi-layered coatings with different cleaning intervention processes were evaluated in terms of the load-depth curves at the load of 10 mN, as shown in Fig. 7. Obviously, the curves were smooth and no pop-in and pop-out events were observed, indicating a good crack resistance and adhesion of the coatings to the substrate under indentation process. As presented in Fig. 7(a), the penetration depths of different coatings were with the normal scope of 184 nm ~190 nm, showing a very small change, which demonstrates that the mechanical properties of three coatings were approximately the same. The hardness (H) and elastic modulus (E) of the three Cr/GLC multi-layered coatings are calculated and shown in Fig. 7(b), which presents that both the H and E has hardly changed after conducting the cleaning intervention with different numbers. The average hardness of three coatings is in the range of 17.21 GPa – 17.92 GPa and the difference among the coatings was no more than 3%. Elastic modulus shares the same characteristics with the hardness with the little changes among the different coatings.

The anti-tribocorrosion performance of coatings with and without conducting the cleaning intervention was assessed with the friction tests at 3.5 wt% solution under OCP condition, as shown in Fig. 8. The friction curves of the coatings are both smooth and kept at a low level after entering the stable sliding period, as shown in Fig. 8(a). The stable friction coefficient is approximately equal (in the range of 0.062–0.069) to each other and the wear rate among them is quite small and differs a little as well. Although the OCP decreased rapidly once the sliding starts for all coatings, the potential drops during the sliding process for each coating was quite small. The decline of the potential often can be considered as a maker for the integrity of the coating during the sliding process, and the maximum decline among these coatings was no more than 0.07 V, demonstrating that all the coating did not peel off during the sliding[20]. The wear track morphologies and corresponding cross-sectional profiles in Fig. 9 show that the three coatings present relatively narrow and shallow wear tracks after tribocorrosion tests,

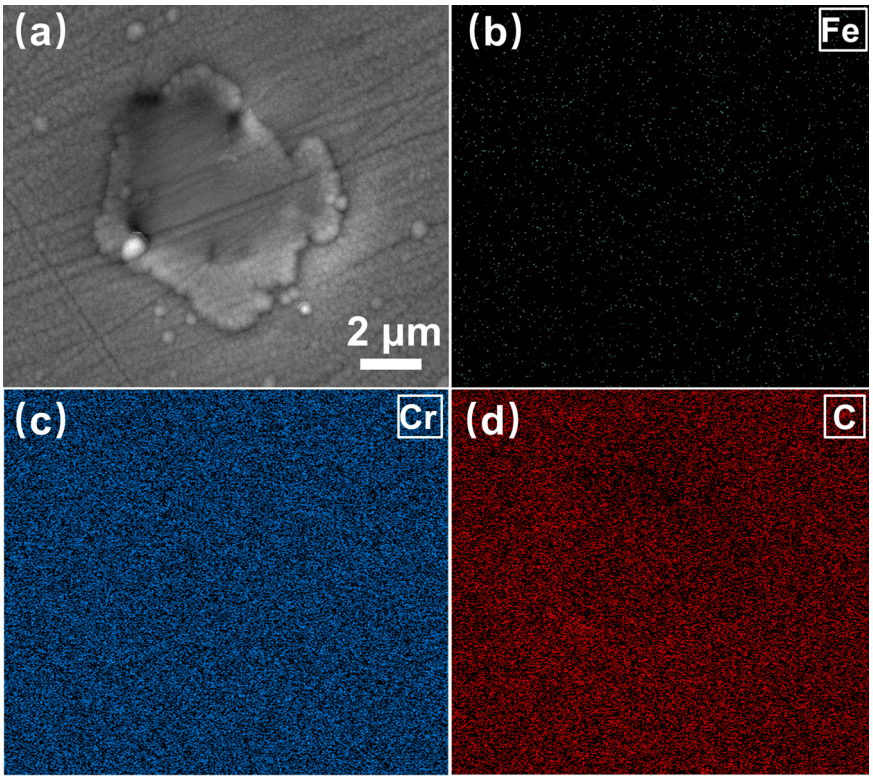

Fig. 6. Surface morphologies and corresponding EDS mapping results of the crater-like defects in S3.

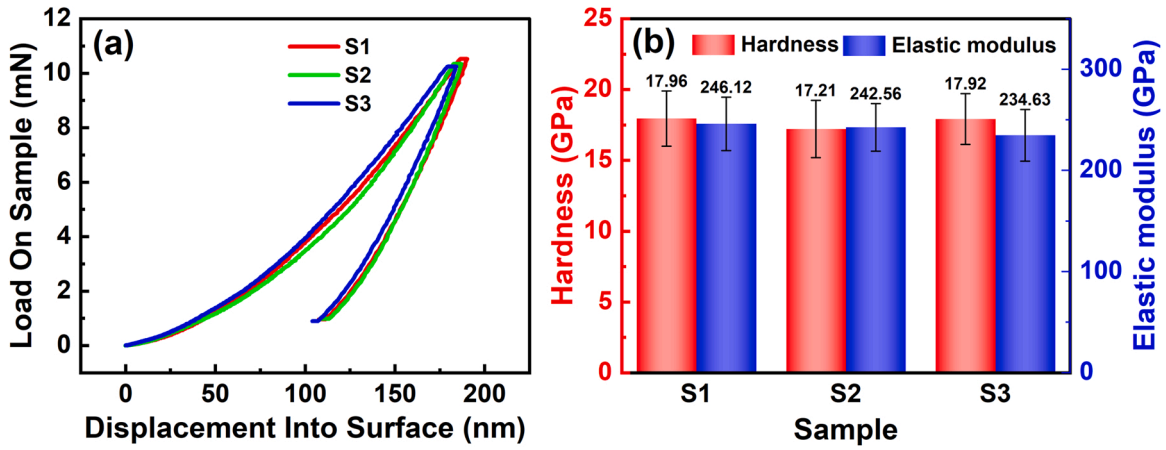

Fig. 7. The indentation curves of the three coatings (a) and the hardness and elastic modulus (b).

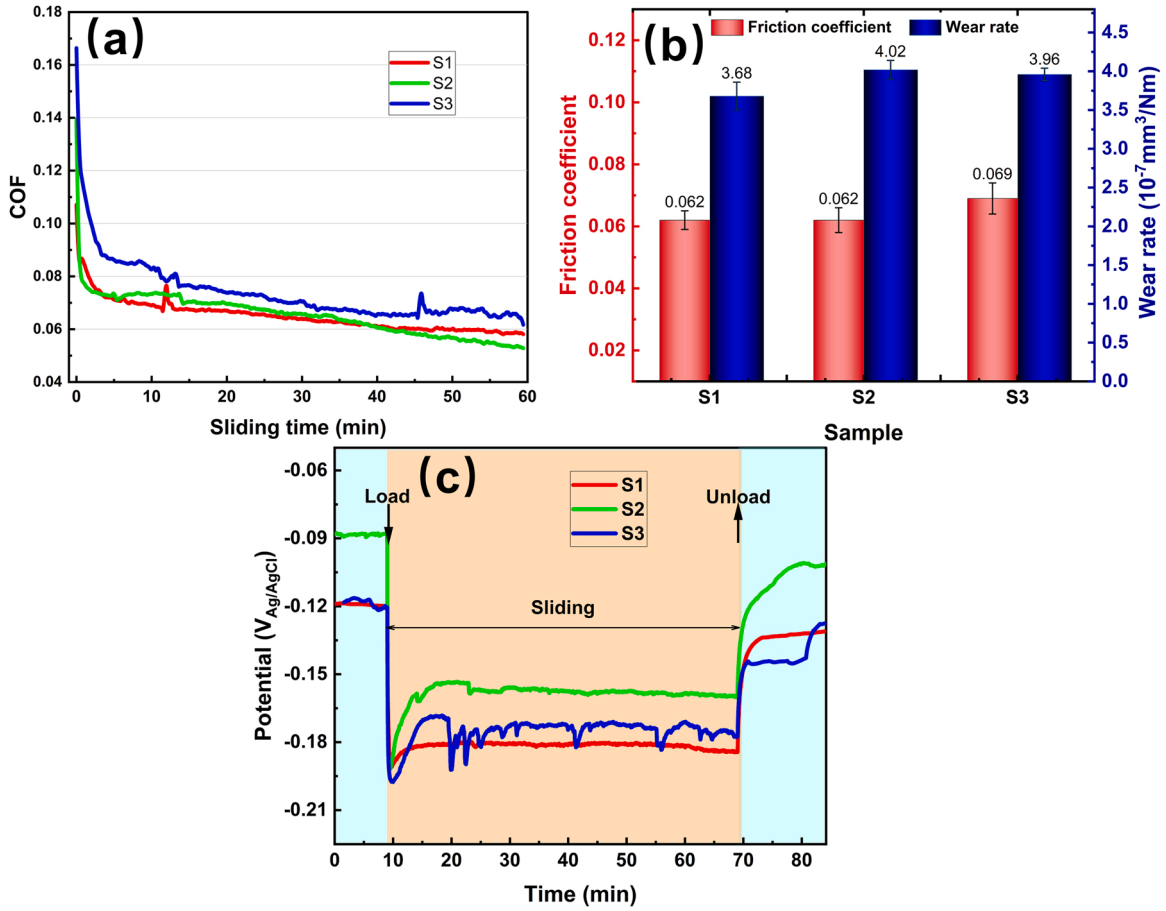

Fig. 8. The friction curves of the three coatings (a), the calculated average coefficient of friction and the wear rate(b), the OCP evolution during the sliding process of different coatings (c).

illustrating that all the coatings have a good anti-tribocorrosion performance with and without cleaning intervention.

In summary, these results strongly suggest that the cleaning intervention processes proposed in this study did not deteriorate the mechanical and tribocorrosion properties of the Cr/GLC multi-layered coatings, which will lay a solid foundation for further research into their corrosion resistance in the simulated deep-sea environment.

3.4. Electrochemical corrosion behaviour

3.4.1. EIS analysis

To investigate the deterioration of the corrosion behaviour of the coatings within a certain period, an immersion test was conducted in a simulated deep-sea environment for 300 h at high hydrostatic pressure of 31 MPa. The EIS tests, before and after the immersion, were conducted to evaluate the evolution of the corrosion resistance. Fig. 10(a) shows the Nyquist plots of the coatings before the immersion tests.

All the plots of the three samples with Cr/GLC multi-layered coatings

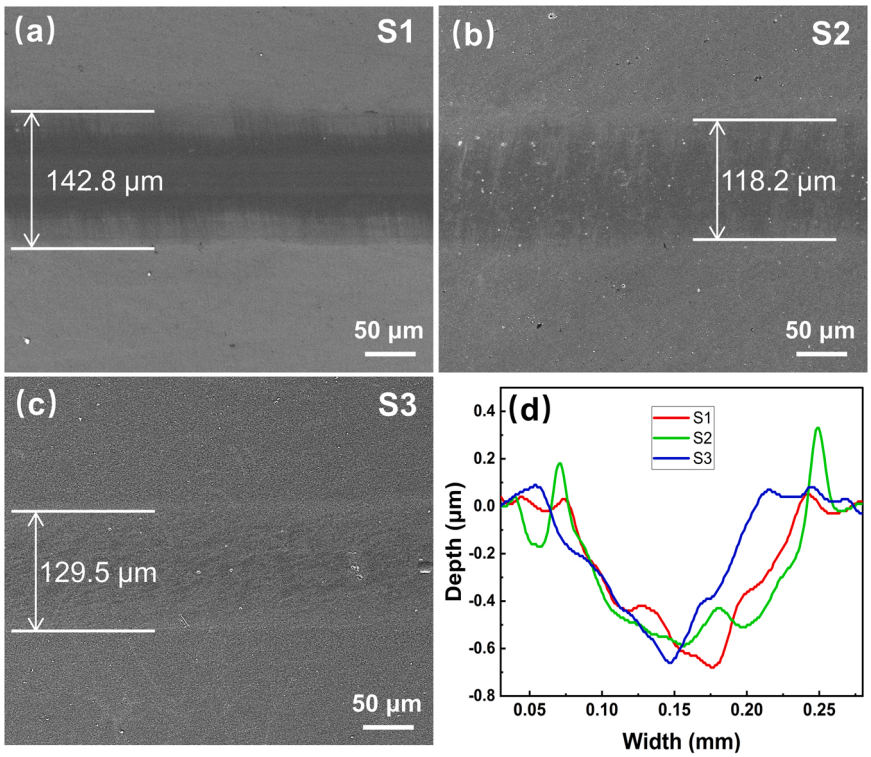

Fig. 9. The wear track morphologies of the three coatings (a)-(c) and the corresponding cross profiles of the wear track under OCP condition.

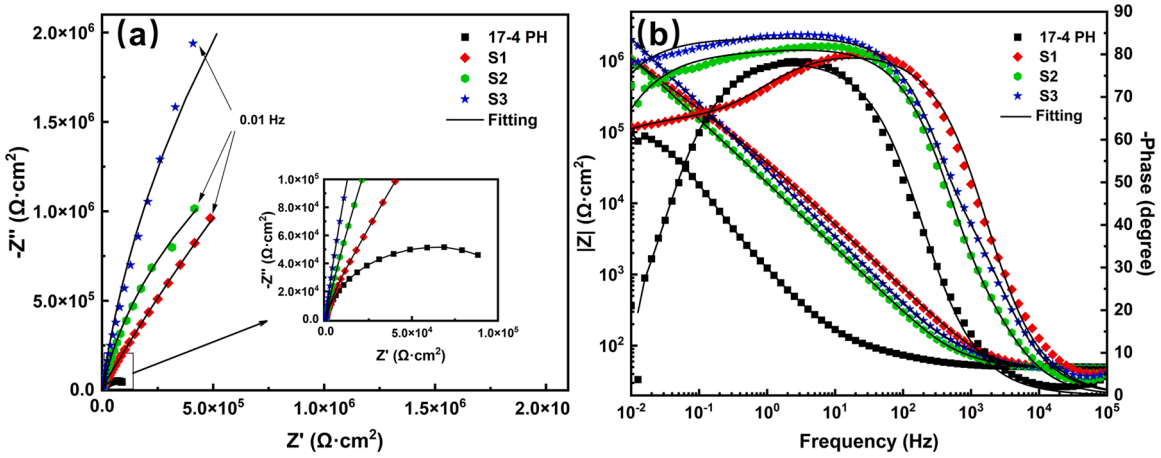

Fig. 10. EIS results of the three samples before the immersion test: (a) Nyquist plots and (b) Bode plots.

presented a remarkably larger capacitance loop than that of the bare substrate in the whole frequency range, indicating the increased protectiveness of all the coated samples. Particularly, regarding the three coated samples, the sequence of the diameters of the capacitive loop was S3 > S2 > S1. The Bode plot (Fig. 10(b)) also intuitively revealed that the sequence of the absolute impedance value, |Z|, was S3 > S2 > S1 > 17–4PH, demonstrating that the S3 sample exhibited the best corrosion resistance after twice cleaning intervention. Moreover, the Bode phase plot (Fig. 10(b)) avails abundant information on the electrochemical responses. Apparently, S3 exhibited a higher and more stable phase-angle maxima (~80°) across a wider frequency region (10^{-2}-10^{2} Hz) compared with the other coatings and substrates. As the capacitive coating, the impedance behaviour of the GLC coating was still capacitive, although the coating comprising growth defects generally deviated from a perfect capacitor, which was mainly due to the interaction of the electrolyte with the substrate through the penetrating defects[46]. In the overall frequency region, the high-frequency capacitive region reflected the response that was related to the coating surface, while the low-frequency capacitive region elucidated the reaction at the interface between the electrolyte and substrate occurring at the bottom of the defects. Although S1 and S2 also exhibited a capacitive region at a low frequency, their phase angle moved towards the lower direction, indicating that they exhibited extensive defects and that localised corrosion occurred at the defect sites.

The most significant factor affecting the corrosion process at the deep-sea environment is the hydrostatic pressure. Our previous research confirmed that the hydrostatic pressure-promoted corrosion process of the GLC coating closely corresponded to the severe interfacial corrosion that was caused by the dramatic diffusion of seawater through the penetrating defects[38]. For a clear comparison, the EIS results (before and after the immersion tests) were plotted together, as shown in Fig. 11. Evidently, the Nyquist plots (Fig. 11(a), (c), and (e)) demonstrated that

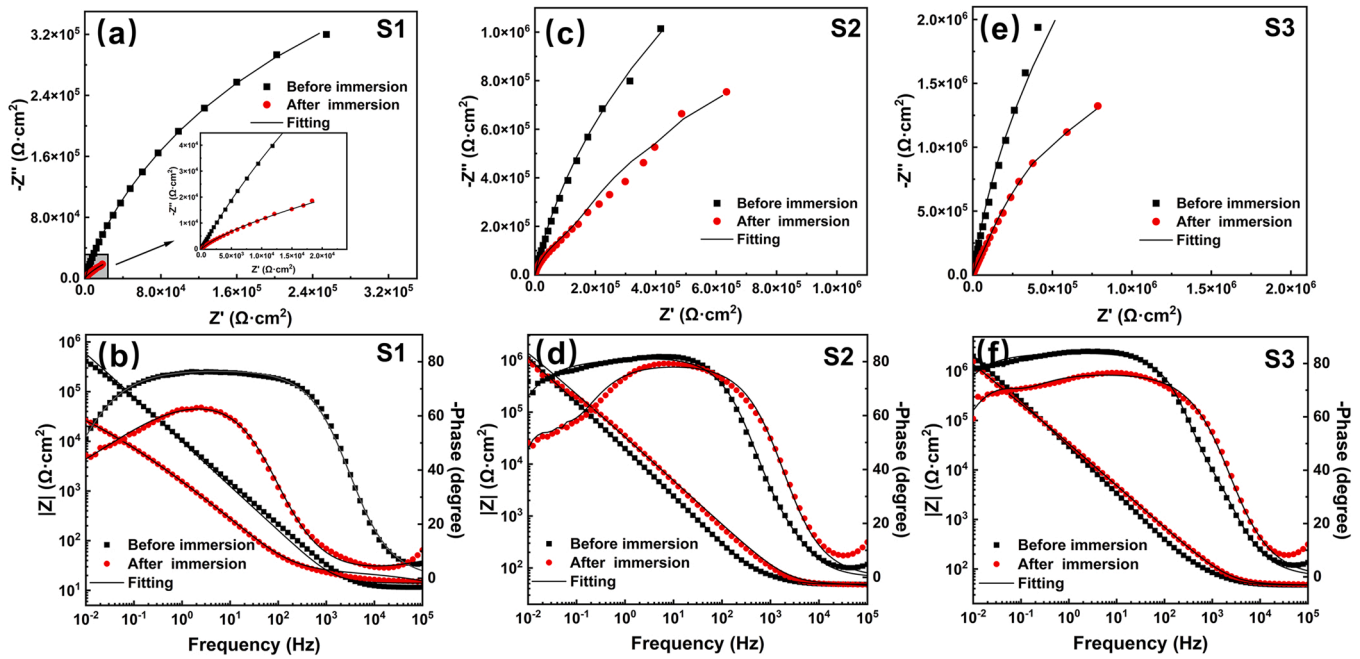

Fig. 11. Nyquist and Bode plots of the three samples before and after the immersion test under the 31-MPa environment for 300 h. (a) and (b) for the S1 coating. (c) and (d) for the S2 coating. (e) and (f) for the S3 coating.

the capacitive loop diameter decreased after the immersion test, indicating a decline in the corrosion resistance of the three samples, following the immersion tests. Moreover, the S1 sample exhibited the most significant decline in capacitance loop diameter compared with the other samples, thus indicating the worst corrosion protectiveness in the deep-sea environment. |Z| in the Bode impedance plots (Fig. 11(b), (d), and(f)) demonstrated a gradually decreasing trend. The Bode phase angle plots indicated that the low-frequency capacitive regions, S1 and S2, shifted more negatively (~40°), while S3 still maintained a relatively high phase angle (~60°). These results indicate that S3 exhibited the least decline, although the corrosion resistance of all three samples decreased after the immersion test, indicating that S3 exhibited the lowest defect density. Therefore, the degree of deterioration of the corrosion resistance for the different samples in harsh deep-sea environments corresponded to their coating density levels. Furthermore, to quantitatively study the evolution of corrosion resistance during the immersion test, all the EIS results were fitted with corresponding equivalent circuits. Based on the features of the Bode phase angle plots (Fig. 10(b)), there were two time constants in the coated samples (S1-S3) and only one time constant in the substrate. Accordingly, the equivalent circuits comprising different time constants are schematically shown in Fig. 12. In these equivalent circuits, R_s is the solution resistance, R_{po} is the coating pore resistance, and R_{ct} is the charge-transfer resistance at the surface of the substrate. Owing to the 'scattering effect', which proceeded from the non-homogeneous nature of the coating surface, the constant phase elements (CPE) were introduced in these models. The impedance of a CPE can be described as follows: [47]:

$$Z_{CPE} = [Y(j2\pi f)^n]^{-1}, \quad (2)$$

where $j = -1^{0.5}$, f is the frequency, n and Y are the parameters of the CPE. The closer the value of 1 of n, the better the capacitive response. Thus, CPE_{dll} is the capacitance of the double layer at the electrolyte/substrate interface, and CPEc is the capacitance of the coating surface. Since ion diffusion always occurs in the defect, a Warburg diffusion element, Z_{diff}, was introduced to represent the diffusion of the corrosive species from the solution into the small defect and from the bottom of the corroding substrate into the solution [48]. According to diffusion theory, the semi-infinite length diffusion element of the Warburg impedance, W, is suitable in this study [49]. Following the possible defect characteristics, which exerts the most significant effect on the diffusion of the electrolyte in the Cr/GLC multi-layered coating, two equivalent circuits are shown in Fig. 12 to fit the EIS results. Fig. 12(a) exhibits one constant phase angle was employed to fit the substrate. Fig. 12(b) shows the corrosion process, which occurred at the penetrating defect, that directly exposed the substrate. Besides, Fig. 12(c) was proposed to fit the results in the non-penetrating defects, which only exposed the Cr interlayers. The fitting data of the measured EIS results are listed in Table 1.

Among these fitting parameters, CPE_c and the R_{pore} were closely related to the corrosion performance of the coating, which was often

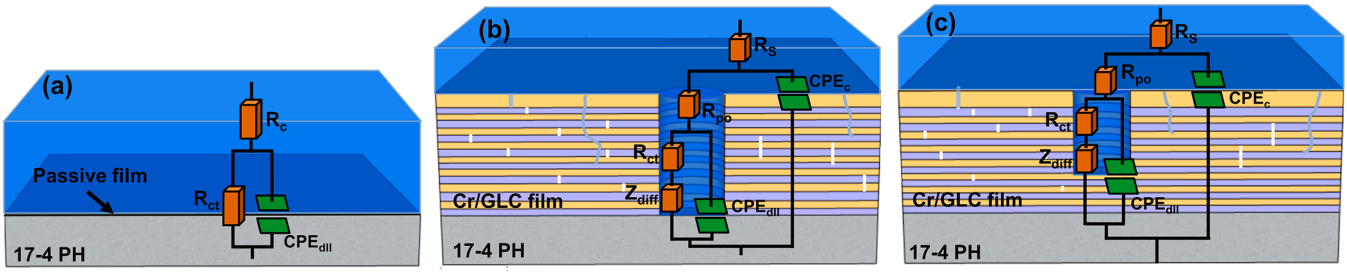

Fig. 12. Equivalent electrical circuit for the (a) bare 17–4PH substrate and Cr/GLC multi-layered coatings(b)-(c).

Table 1
Fitting parameters of the EIS results employing the equivalent circuits.

	17–4PH	S1		S2		S3	
		Before immersion	After immersion	Before immersion	After immersion	Before immersion	After immersion
R_s ($\Omega\cdot cm^2$)	15.1	47.7	15.5	48.1	47.9	47.6	47.4
CPE_c ($\Omega^{-2}cm^{-2}S^{-n}$) ($\times10^{-6}$)	35.80	15.25	61.8	1.71	5.53	2.18	6.17
n_c	0.884	0.992	0.832	0.907	0.881	0.936	0.842
R_c($\Omega\cdot cm^2$)	\	47.3	51.3	141.3	130.3	171.3	140.3
CPE_{dll} ($\Omega^{-2}cm^{-2}S^{-n}$) ($\times10^{-6}$)	\	3.69	1.38	1.77	0.47	2.12	0.07
n_{dll}		0.845	0.778	0.992	0.656	0.957	0.511
R_{ct} ($M\Omega\cdot cm^2$)$\times$ 10^6	1.24	0.768	0.68	1.55	0.80	1.84	1.02
Y_0($\mu/cm^2s^{1/2}S$)		2.36	5.62	1.39	6.03	0.45	0.95
χ^2 ($\times10^{-4}$)	1.23	9.32	6.36	2.70	0.29	3.70	0.19

employed to analyse the microstructure of the coating during the corrosion process. In this study, CPE_c was mainly determined by the microstructure of the top GLC coating, which can be expressed by the following equation according to the parallel-plate model [50]:

$$CPE_C = \frac{\gamma\varepsilon_c\varepsilon_0(1-P)A}{d}, \tag{3}$$

where γ is the surface roughness factor, ε_0 is the permittivity of the free space (8.845×10^{-12} F/m), ε_c is the dielectric constant of the coating, P_p is the porosity of the coating, A is the exposed coating area in the tests (1.13 cm^2), and d is the coating thickness. Assuming that the coating was sufficiently inert in artificial seawater, it could be reasonably speculated that the surface factors, γ and d, were constant during the tests. Similarly, ε_c remained stable because an identical coating was adopted in the immersion test. Therefore, CPE_C was mainly related to P_P. A higher P_p increased the exposed area in the electrolyte and produced increased coating capacitance. Table 1 indicates that S1 exhibited a larger coating capacitance value compared with S2 and S3 before the immersion, and this agrees with the calculated results of P_p. After the immersion tests, all the CEP_C values increased accordingly, and this was related to the hydrostatic pressure-promoted diffusion process through the defects[38].

R_p is the resistance due to the current flow through the pores [51]. Here, R_p essentially originated from the diffusion resistance of the ions (Fe^{2+} and Cr^{3+}) through the penetrating or crater-like defects that exposed the substrate or Cr interlayers, respectively.

$$R_{pore} = \rho\frac{L}{A_p}, \tag{4}$$

where ρ is the solution resistance to the defects and L and A_p are the lengths of the defects and the defect area, respectively. The maximum L was equal to the coating thickness only if the defect corresponded to the through-thickness; L was lower in the other cases. Accordingly, it is reasonable to deduce that A_p in S3 was smaller than that in S1 and S2, indicating that the cleaning intervention could effectively seal the penetrating defects in the coatings. This finding is supported by the results of the calculated protective efficiency and P_P in the polarization curves. R_{ct} decreased after the immersion tests, but S3 still maintained a relatively high value (1.02 $M\Omega\cdot cm^2$). Furthermore, the n-closeness value that was associated with CPE_{dll} was gradually far from 1, indicating the severe and persistent localised corrosion processes in the low-frequency region. Regarding the diffusion process through the defects, the mathematical expressions of Z_{diff} can be described by the following equation [52]:

$$Z_{diff} = \sigma_w(\omega)^{-1/2}(1-j) \tag{5}$$

where σ_ω is the Warburg coefficient. Thus, σ_w was inversely proportional to the magnitude of the admittance, Y_0, as presented in Table 1. Furthermore, σ_w can be further defined by the following equation:

$$\sigma_\omega = \frac{RT}{n^2F^2A\sqrt{2}}\left(\frac{1}{C_o\sqrt{D_O}}+\frac{1}{C_R\sqrt{D_R}}\right) \tag{6}$$

where ω is the radial frequency; D_0 and D_R are the diffusion coefficients of the oxidant and reductant, respectively; n is the number of participating electrons; C_0 and C_R are the concentrations of the oxidant and reductant, respectively; F is the Faraday constant; R is the gas constant; T is the temperature; and A is the surface area of the electrode. Particularly, A is the defect area in the coating in this study. The high value of the Y_0 in S1 indicated that the defect area therein was larger than those in S2 and S3, further demonstrating that a better sealing efficiency was endowed with counting the cleaning intervention. Further, Y_0 slowly increased after the immersion tests owing to the corrosion process that occurred at the bottom of the substrate or exposed Cr interlayers. In this case, the anodic process injects metal ions from the substrate into the electrolyte, and such a process also reduces R_{po}.

3.4.2. Analysis of the polarization curves

The cleaning intervention during the alternative deposition changed the structure of the defect, thus significantly altering the corrosion behaviour of the coating in the harsh deep-sea environment. Owing to the good electrochemical inertness of the GLC coating in seawater, the coating was cathodic to the metal substrate. Fig. 13 shows the potentiodynamic polarization curves, as well as the calculated results before the immersion test in the simulated deep-sea environment, they demonstrated quite different electrochemical responses. Apparently, the potentiodynamic polarization curves (Fig. 14(a) indicated that all the coated samples (S1-S3) demonstrated significant improvements regarding their corrosion resistances as the corrosion current was two orders of magnitude lower in the anodic domain. Nonlinear least-square method was used to fit the three curves obtained from the Cr/GLC multilayered coatings and the curve of 17–4PH stainless steel was fitted with Tafel extrapolation due to the existence of a Tafel region in an anode domain. The corresponding parameters from the potentiodynamic polarization curves were listed in Table 2.

The polarization resistance R_p value of each sample was calculated employing the Stern-Geary equation [53]:

$$R_p = \frac{\beta_a\beta_c}{2.303i_{corr}(\beta_a+\beta_c)A} \tag{7}$$

where β_a and β_c are the anodic and cathodic Tafel polarization slopes, respectively; i_{corr} is the corrosion current density; and A, which is 1.13 cm^2 in this study, is the exposed area of all the samples during the tests. Table 2 reveals that the coated samples exhibited a higher corrosion potential (E_{corr}) and a lower corrosion density (i_{corr}). R_P increased with the increasing number of cleaning intervention cycles, indicating that increased numbers of cleaning interventions would ensure better corrosion resistance of the coating. Regarding the cathodic polarization curves of the three Cr/GLC multi-layered coatings, a detailed analysis revealed that the region of the cathodic domain displayed the same oxygen-reduction behaviours, indicating that oxygen reduction

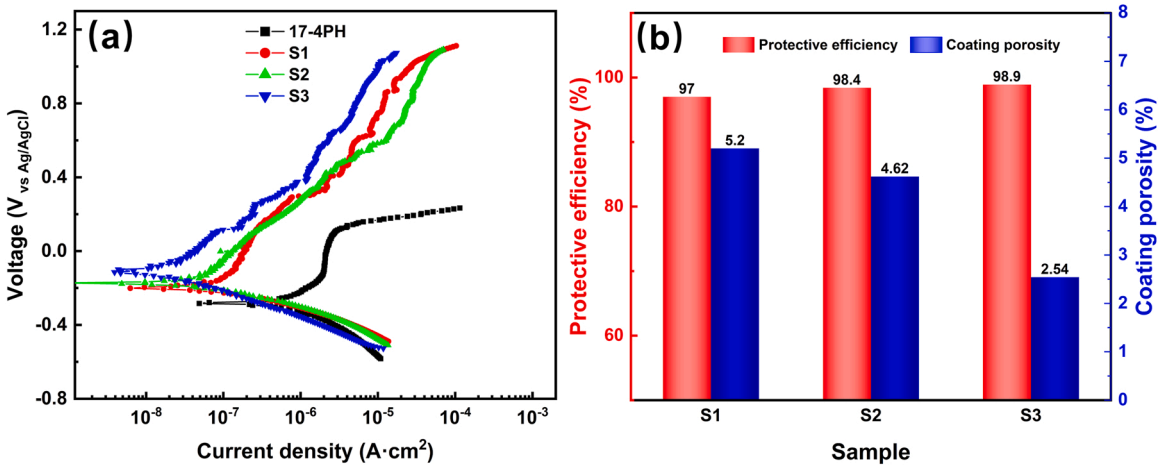

Fig. 13. Potentiodynamic polarization curves (a), the calculated protective efficiency and porosity of the Cr/GLC multi-layered coatings without immersion tests (b).

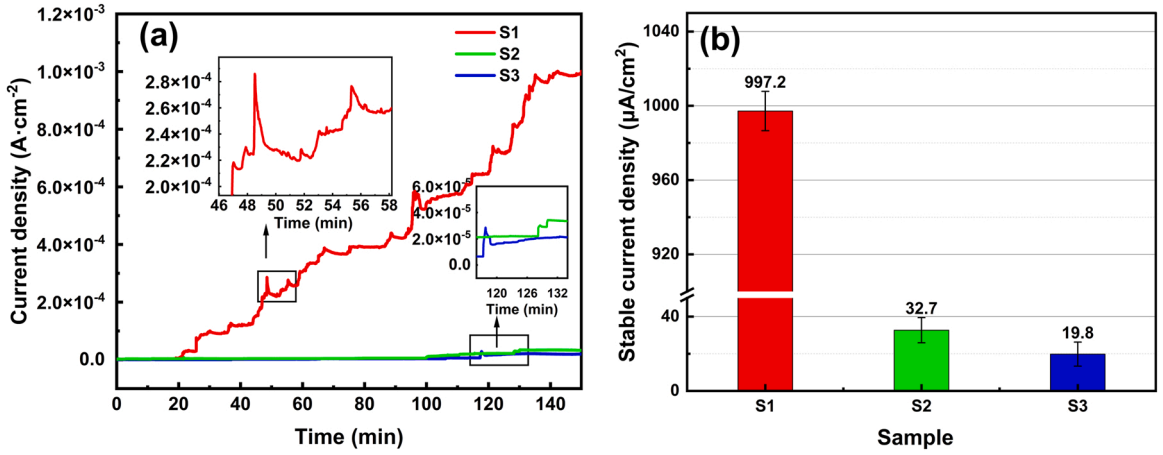

Fig. 14. Potentiostatic polarization curves of the three coatings at 0.4 Vvs OCP for 150 min (a) and the corresponding extracted corrosion current density at the final stable period (b).

Table 2
Electrochemical parameters of the samples from the polarization curves.

Sample	E_{corr} V (vs Ag/AgCl)	i_{corr} 10^{-8}A/cm^2	β_a mV/decade	β_c mV/decade	R_p MΩ·cm^2
S1	-0.197	4.88	373	-104	1.36
S2	-0.177	2.66	292	-91	1.53
S3	-0.097	1.17	306	-96	2.62
17–4PH	-0.289	163.92	2163	-353	0.08

dominated the cathodic process and that the corrosion process was quite weak. Moreover, the corrosion potential increased with the increasing cleaning intervention times, and the as-deposited coating (S1) sample exhibited the lowest E_{corr} value of approximately − 0.197 $V_{vs\ Ag/AgCl}$. It is well known that the two following aspects account for the reduced corrosion potential in the corrosive media: the acceleration of anodic corrosion or its inhibition [54,55]. According to the foregoing analysis of almost the same cathodic process, it could be deduced that the acceleration of the anodic dissolution process properly explained the decrease in the corrosion potential.

Accordingly, all the anodic polarization curves of the three samples demonstrated distinctly active corrosion features, indicating a completely different anodic dissolution process compared with that in the 17–4PH stainless steel, which exhibited a typical passive region. In this study, the Cr/GLC multi-layered coating contained metal Cr interlayers and an inert atmospheric carbon layer, and the exposed substrate at the penetrating defects could be corroded in the electrolyte and Cr interlayers. Although Cr is a passive metal, its coatings and those of its nitrides in seawater generally exhibit active dissolution characteristics [44,56–58]. Consequently, it could be deduced that the anodic corrosion current was initiated at the substrate and Cr interlayers. Crues [26] reported that the mixed potential concept is an appropriate method for defining the defect density of the coated sample. The corrosion current that was detected in the GLC-coated samples essentially corresponds to the leakage current since it originated from the anodic dissolution at the bottom of the defect that exposed the substrate or Cr interlayers. The determination of the porosity is crucial to estimating the overall corrosion protection performance of the coatings. The protective efficiency (P_e) and P_P of the three samples are generally calculated employing the following empirical equations [48]:

$$P_e = 100\left(1 - \frac{i_{corr}}{i^0_{corr}}\right) \tag{8}$$

$$P_P = \left(\frac{R_{p(substrate)}}{R_{p(coating)}}\right) 10^{\left(-\frac{|\Delta E|}{\beta_a}\right)} \tag{9}$$

where i_{corr} and i^0_{corr} are the corrosion current densities with and without the coatings, respectively; $R_{p(substrate)}$ and $R_{p(coating)}$ are the polarization resistances of the substrate and coated sample, respectively; $|\Delta E|$ is the

absolute value of the potential difference between the free corrosion potentials of the coating sample and the substrate; and β_a is the slope of the anodic polarization curve of the substrate. According to Eqs. (8) and (9), The protective efficiency and P_P are shown in Fig. 13(b). S3, which underwent two cleaning interventions during the alternative deposition, exhibited the highest protective efficiency (98.9%) and lowest P_P (2.54%), demonstrating that the cleaning intervention is a feasible strategy for decreasing the penetrating defects in the coating and that many cleaning interventions were required to produce better corrosion protection performance.

To further verify the anti-localised corrosion properties of the optimised coatings, the potentiostatic polarization tests were conducted in the atmospheric environment at a constant potential (0.4 $V_{Ag/AgCl}$) over a stable OCP value for 150 min Fig. 14 shows the current density-time curves and extracted stable corrosion current density results of the three coatings. Regarding the as-deposited coating of S1, its corrosion current density remained stable only during the initial 20 min before it rapidly increased. Contrarily, the current densities of S2 and S3 displayed significantly stable characteristics over the test period, indicating that the cleaning intervention significantly decreased the penetrating defect density of the coating. Furthermore, the curve of S1 presented abundant current transients, and the top-left inset of Fig. 14(a) clearly shows a typical characteristic of this current peak. Regarding the pure protective feature of the GLC layer in this study, the current signal was due to the interaction between the substrate and electrolyte or the Cr interlayer and electrolyte through the defects. According to the peak features of these transients, the presence of the current transients in S1 might be mainly related to the transformation from the metastable to stable pitting corrosions in the substrate. Notably, the inset at the right bottom of Fig. 14(a) shows the step-up features of the current densities of S2 and S3 towards the end of the test, and this corresponds to the diffusion of the electrolyte through several tiny pores to produce slightly localised corrosion. The stable current densities of S2 and S3, which underwent cleaning interventions, exhibited remarkably lower corrosion currents than that of S1 over the test period (Fig. 14(b)). More importantly, S3, which underwent two cleaning interventions, exhibited the lowest current density (19.8 μA/cm^2), indicating that the more the cleaning interventions, the lower the densities of the penetrating defects in the coatings.

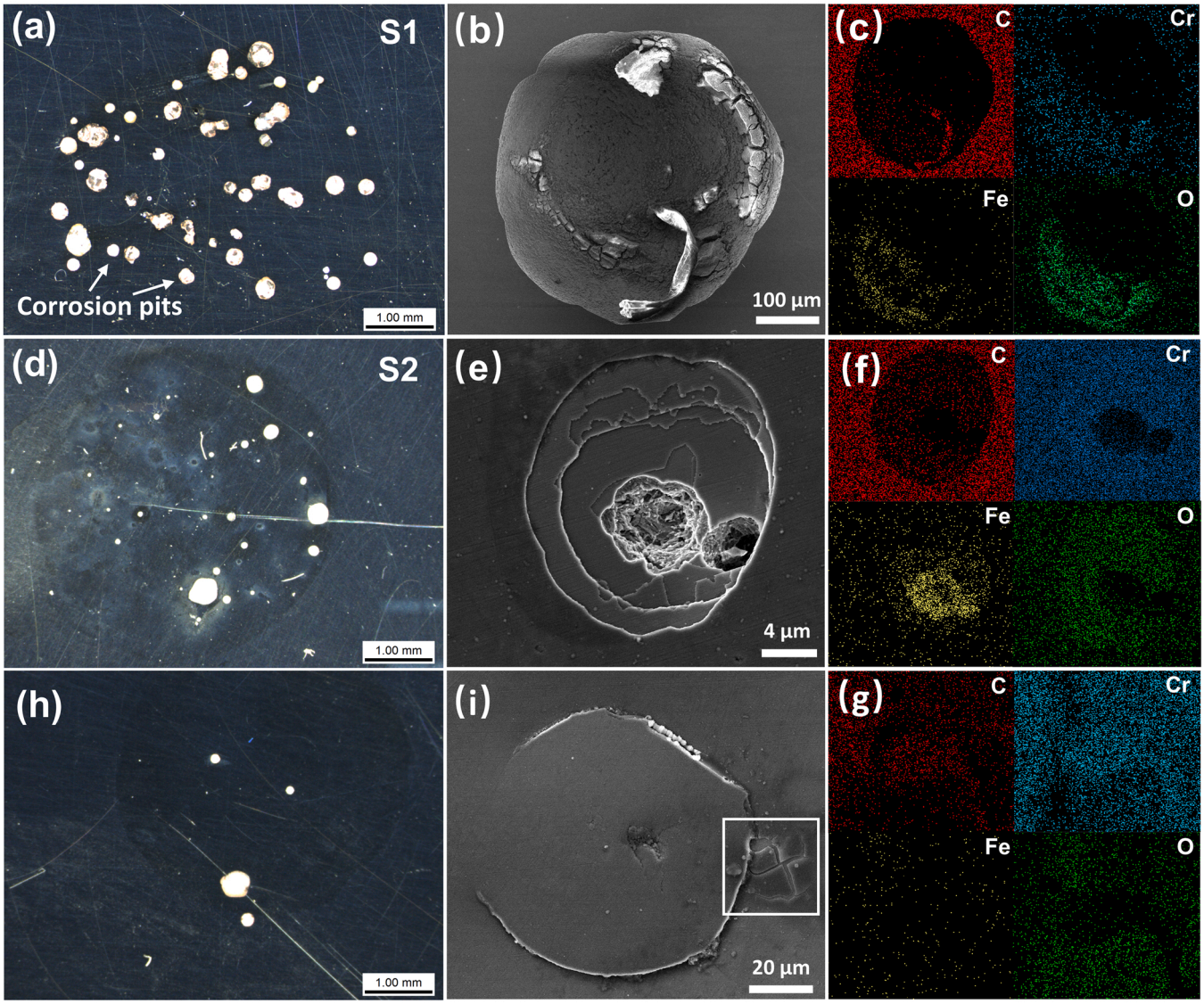

Fig. 15. Corrosion morphologies and corresponding EDS mapping results of the coatings after the potentiostatic polarization tests. (a), (d), and (h) are the optical corrosion morphologies of the three coating after the tests; (b), (e), and (i) are the typical SEM corrosive images obtained from the corresponding OM images; and (c), (f), and (g) are the corresponding EDS mapping of the corrosive sites.

3.5. Analysis of the corrosion morphologies

Fig. 15 shows the optical microscopy (OM) and SEM morphologies of the corroded Cr/GLC multi-layered coating after the potentiostatic polarization tests. The OM morphologies (Fig. 15(a), (d), and (h)) revealed different corrosion deterioration characteristics. S1, which did not undergo the cleaning intervention, exhibited numerous of visible corrosion pits with an average diameter of ~500 μm. The typical SEM image of the morphology of the corrosion pit (Fig. 15(b)), as extracted from Fig. 15 (a), shows that the complete detachment of the Cr/GLC coating and the severe corrosion of the substrate.

The EDS mapping results (Fig. 15(c)) show that the residues were partial coatings. These topographic characteristics correlate with the corrosion current density (Fig. 15(b)). However, the situation was significantly better, following the cleaning interventions on the Cr/GLC multi-layered coatings. S2 and S3 exhibited fewer visible corrosion pits compared with S1. Fig. 15(d) shows that majority of the corrosion pits were much smaller, except for some. The detailed SEM morphology of the tiny corrosion pits (Fig. 15(e)) revealed that only a small area of the substrate was corroded (Fig. 15(f)) and that the coating was detached layer by layer. This is a typical medium-term localised corrosion process induced by the penetrating defect. The electrolyte reached the substrate, after which anodic dissolution occurred. Dissimilar to Fig. 15(b), the defect here exhibited a smaller diameter, which allowed a small amount of the electrolyte to diffuse to the substrate. Furthermore, the coating with two cleaning interventions exhibited the least corrosion pits in the test area as only four visible pits were observed (Fig. 15(h)). The details of the initial localised corrosion process (Fig. 15(i)) might avail abundant specific information about the origin of localised corrosion. This localised corrosion is an imperfection that exposed the Cr interlayer. Severe interface corrosion occurred at the Cr layer, and many corrosion products were produced at the interface. The accumulation of corrosion products caused the stress concentration between the interface and further caused the cracking of the coating. The corrosion process that developed along a deep direction through the penetrating defect causes the catastrophic failure of the coating. Thus, decreasing the penetrating defect density in the coating is crucial to enhancing the localised corrosion resistance of the coating for application in deep-sea environments.

In summary, the corrosion model of the Cr/GLC multi-layered coating, following the cleaning interventions, was proposed in this study, following the morphologies of the defects and the electrochemical corrosion results under different conditions. The penetrative defects were generally induced by the detachment of the nodular-like defects during or after the deposition process. Therefore, successive deposition processed without external cleaning intervention would cause the formation of penetrative defects in the coating. Such defects would account for severe localised corrosion on the substrate, which would cause the catastrophic failure of the coating, as presented in Fig. 16. After conducting the cleaning intervention during the deposition, the seeds in the Cr interlayers or the formed tiny nodular-like defects would be detached, leaving a crater behind the nodules. Therefore, the following deposition can effectively seal the crater in the former several layers and produce a denser multi-layered coating after the deposition. After the deposition process, some nodular-like defects were detached owing to the current or cleaning intervention, although the exposed layer would always be the passive Cr interlayer, which still exhibited good corrosion protection in the electrolyte.

4. Conclusions

Here, we proposed a method for reducing the penetrating defect density of typical Cr/GLC multi-layered coating by introducing cleaning interventions during the deposition process with different numbers of times. The microstructures of the defect were evaluated before and after the cleaning interventions in detail, and the corresponding corrosion behaviours of the different coatings under atmospheric and deep-sea conditions were analysed thoroughly. The results demonstrated that the introduction of the cleaning intervention does not deteriorate the mechanical and tribocorrosion properties of the coatings, but significantly decreases the penetrating defect density and changed the forms of the defects. The localized corrosion resistance was significantly improved under the atmospheric and hydrostatic pressure conditions. These results indicated that the cleaning intervention is a promising strategy for further enhancing localised corrosion in a harsh deep-sea environment.

CRediT authorship contribution statement

Yingrui Liu and Shuyu Li contributed to this work equally. **Yingrui Liu:** Conceptualization, Methodology Investigation, Validation and Writing – original draft. **Shuyu Li:** Methodology, Investigation,

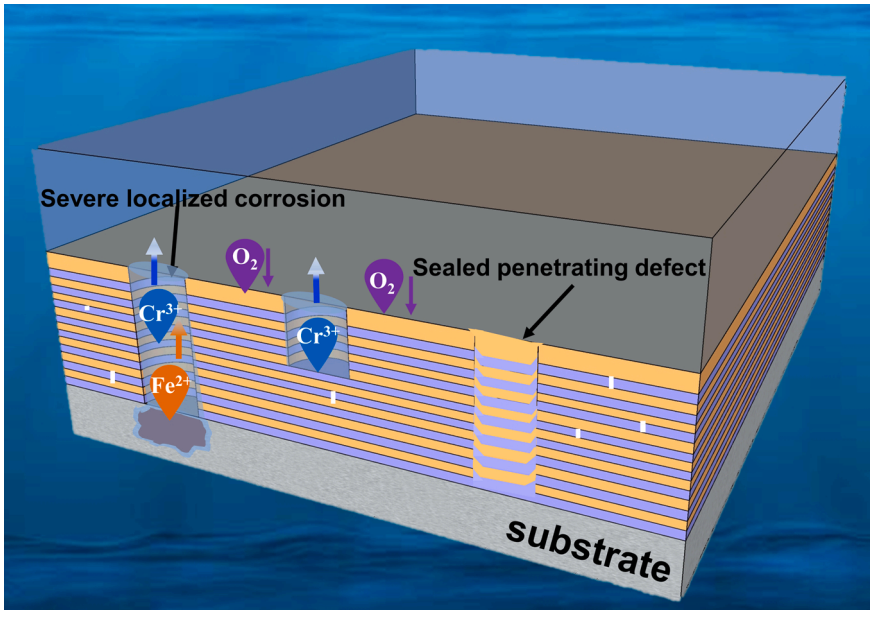

Fig. 16. The corrosion model of the Cr/GLC multi-layered coating in simulated deep-sea environment.

Validation. **Hao Li:** Methodology. **Guanshui Ma:** Methodology Investigation. **Peng Guo:** Visualization. **Lili Sun:** Methodology, Investigation. **Peiling Ke:** Writing – review & editing, Supervision, Funding acquisition. **Kwang-Ryeol Lee:** Conceptualization, Methodology. **Aiying Wang**: Writing – review & editing, Funding acquisition, Supervision. All authors are cussed the results and commented on the manuscript.

Declaration of Competing Interest

The authors declare that they have no known competing financial interests or personal relationships that could have appeared to influence the work reported in this paper.

Acknowledgements

This work was financial supported by A-class pilot of the Chinese Academy of Sciences (XDA22010303), National Science Fund for Distinguished Young Scholars of China (52025014), CAS-NST Joint Research Project (174433KYSB20200021), CAS Interdisciplinary Innovation Team (292020000008), K.C.Wong Education Foundation of Chinese Academy of Science (GJTD-2019-13). KR was financially supported by the 2020 NST-CAS Collaboration Program (2N45610) of the National Research Council of Science and Technology of Korea.

Appendix A. Supporting information

Supplementary data associated with this article can be found in the online version at doi:10.1016/j.corsci.2022.110175.

References

[1] T. Duan, W. Peng, K. Ding, W. Guo, J. Hou, W. Cheng, S. Liu, L. Xu, Long-term field exposure corrosion behavior investigation of 316L stainless steel in the deep sea environment, Ocean Eng. 189 (2019), 106405, https://doi.org/10.1016/j.oceaneng.2019.106405.
[2] S.N. Verichev, V.V. Mishakin, D.A. Nuzhdin, E.N. Razov, Experimental study of abrasive wear of structural materials under the high hydrostatic pressure, Ocean Eng. 99 (2015) 9–13, https://doi.org/10.1016/j.oceaneng.2015.03.001.
[3] J. Teague, M.J. Allen, T.B. Scott, The potential of low-cost ROV for use in deep-sea mineral, ore prospecting and monitoring, Ocean Eng. 147 (2018) 333–339, https://doi.org/10.1016/j.oceaneng.2017.10.046.
[4] D. Leng, S. Shao, Y. Xie, H. Wang, G. Liu, A brief review of recent progress on deep sea mining vehicle, Ocean Eng. (2021), 108565, https://doi.org/10.1016/j.oceaneng.2020.108565.
[5] F.W. Fink, Corrosion of metals in sea water, in: Saline Water Conversion, American Chemical Society, 1960, pp. 27–39.
[6] M. Abbas, M. Shafiee, An overview of maintenance management strategies for corroded steel structures in extreme marine environments, Mar. Struct. 71 (2020), 102718, https://doi.org/10.1016/j.marstruc.2020.102718.
[7] E. Canepa, R. Stifanese, L. Merotto, P. Traverso, Corrosion behaviour of aluminium alloys in deep-sea environment: a review and the KM3NeT test results, Mar. Struct. 59 (2018) 271–284, https://doi.org/10.1016/j.marstruc.2018.02.006.
[8] L. Jie, L. Xiang-Bo, W. Jia, L. Tian-Yuan, W. Xiao-Ming, Studies of impedance models and water transport behaviours of epoxy coating at hydrostatic pressure of seawater, Prog. Org. Coat. 76 (2013) 1075–1081, https://doi.org/10.1016/j.porgcoat.2013.03.006.
[9] H.Y. Su, Y. Liang, S.C. Wei, Y.J. Wang, B. Wang, H. Tong, Couple effect of hydrostatic pressure and dissolved oxygen on corrosion behaviour of low-alloy high strength steel in 3.5 wt% NaCl solution, Corros. Eng. Sci. Technol. 54 (2019) 330–338, https://doi.org/10.1080/1478422x.2019.1590959.
[10] C. Zhang, Z.-W. Zhang, L. Liu, Degradation in pitting resistance of 316L stainless steel under hydrostatic pressure, Electrochim. Acta 210 (2016) 401–406, https://doi.org/10.1016/j.electacta.2016.05.169.
[11] S. Hu, L. Liu, Y. Cui, Y. Li, F. Wang, Influence of hydrostatic pressure on the corrosion behavior of 90/10 copper-nickel alloy tube under alternating dry and wet condition, Corros. Sci. 146 (2019) 202–212, https://doi.org/10.1016/j.corsci.2018.10.036.
[12] P. Ren, H. Meng, Q. Xia, Z. Zhu, M. He, Influence of seawater depth and electrode potential on the tribocorrosion of Ti6Al4V alloy under the simulated deep-sea environment by in-situ electrochemical technique, Corros. Sci. 180 (2021), https://doi.org/10.1016/j.corsci.2020.109185.
[13] F. Meng, L. Liu, Y. Li, F. Wang, Studies on electrochemical noise analysis of an epoxy coating/metal system under marine alternating hydrostatic pressure by pattern recognition method, Prog. Org. Coat. 105 (2017) 81–91, https://doi.org/10.1016/j.porgcoat.2016.11.025.
[14] W. Tian, F. Meng, L. Liu, Y. Li, F. Wang, Lifetime prediction for organic coating under alternating hydrostatic pressure by artificial neural network, Sci. Rep. 7 (2017) 40827, https://doi.org/10.1038/srep40827.
[15] Z. Guan, D. Wu, Q. Cheng, Z. Wang, M. Tang, Y. Liu, Friction and wear characteristics of CF/PEEK against 431 stainless steel under high hydrostatic pressure water lubrication, Mater. Des. 196 (2020), https://doi.org/10.1016/j.matdes.2020.109057.
[16] Z. Li, H. Yu, D. Sun, The tribocorrosion mechanism of aluminum alloy 7075-T6 in the deep ocean, Corros. Sci. (2021), https://doi.org/10.1016/j.corsci.2021.109306.
[17] D. Wu, Z. Guan, Q. Cheng, W. Guo, M. Tang, Y. Liu, Development of a friction test apparatus for simulating the ultra-high pressure environment of the deep ocean, Wear 452–453 (2020), 203294, https://doi.org/10.1016/j.wear.2020.203294.
[18] S. Khamseh, E. Alibakhshi, B. Ramezanzadeh, M.G. Sari, A.K. Nezhad, Developing a graphite like carbon:niobium thin film on GTD-450 stainless steel substrate, Appl. Surf. Sci. 511 (2020), https://doi.org/10.1016/j.apsusc.2020.145613.
[19] K. Bewilogua, D. Hofmann, History of diamond-like carbon films - From first experiments to worldwide applications, Surf. Coat. Technol. 242 (2014) 214–225, https://doi.org/10.1016/j.surfcoat.2014.01.031.
[20] X. Sui, R. Xu, J. Liu, S. Zhang, Y. Wu, J. Yang, J. Hao, Tailoring the tribocorrosion and antifouling performance of (Cr, Cu)-GLC coatings for marine application, ACS Appl. Mater. Interfaces 10 (2018) 36531–36539, https://doi.org/10.1021/acsami.8b12359.
[21] N.W. Khun, E. Liu, X.T. Zeng, Corrosion behavior of nitrogen doped diamond-like carbon thin films in NaCl solutions, Corros. Sci. 51 (2009) 2158–2164, https://doi.org/10.1016/j.corsci.2009.05.050.
[22] H. Li, P. Guo, D. Zhang, L. Liu, Z. Wang, G. Ma, Y. Xin, P. Ke, H. Saito, A. Wang, Interface-induced degradation of amorphous carbon films/stainless steel bipolar plates in proton exchange membrane fuel cells, J. Power Sources 469 (2020), 228269, https://doi.org/10.1016/j.jpowsour.2020.228269.
[23] O. Jarry, C. Jaoul, P. Tristant, T. Merle-Mejean, M. Colas, C. Dublanche-Tixier, H. Ageorges, C. Lory, J.-M. Jacquet, Tribological behaviour of diamond-like carbon films used in automotive application: a comparison, Plasma Process. Polym. 6 (2009) S478–S482, https://doi.org/10.1002/ppap.200931007.
[24] H. Miya, J. Wang, Corrosion protect DLC coating on steel and Hastelloy, Mater. Trans. 49 (2008) 1333–1337, https://doi.org/10.2320/matertrans.MRA2007301.
[25] S.H. Ahn, J.H. Lee, J.G. Kim, J.G. Han, Localized corrosion mechanisms of the multilayered coatings related to growth defects, Surf. Coat. Technol. 177–178 (2004) 638–644, https://doi.org/10.1016/s0257-8972(03)00939-3.
[26] J. Creus, H. Mazille, H. Idrissi, Porosity evaluation of protective coatings onto steel, through electrochemical techniques, Surf. Coat. Technol. 130 (2000) 224–232, https://doi.org/10.1016/s0257-8972(99)00659-3.
[27] Z. Wang, C. Wang, Q. Wang, J. Zhang, Electrochemical corrosion behaviors of a-C: H and a-C: N-X: H films, Appl. Surf. Sci. 254 (2008) 3021–3025, https://doi.org/10.1016/j.apsusc.2007.10.088.
[28] R. Shanna, P.K. Barhai, N. Kumari, Corrosion resistant behaviour of DLC films, Thin Solid Films 516 (2008) 5397–5403, https://doi.org/10.1016/j.tsf.2007.07.099.
[29] E. Harkonen, I. Kolev, B. Diaz, J. Swiatowska, V. Maurice, A. Seyeux, P. Marcus, M. Fenker, L. Toth, G. Radnoczi, M. Vehkamaki, M. Ritala, Sealing of hard CrN and DLC coatings with atomic layer deposition, ACS Appl. Mater. Interfaces 6 (2014) 1893–1901, https://doi.org/10.1021/am404906x.
[30] E. Marin, A. Lanzutti, L. Paussa, L. Guzman, L. Fedrizzi, Long term performance of atomic layer deposition coatings for corrosion protection of stainless steel, Mater. Corros. 66 (2015) 907–914, https://doi.org/10.1002/maco.201408012.
[31] K. Bobzin, N. Bagcivan, S. Theiß, R. Weiß, U. Depner, T. Troßmann, J. Ellermeier, M. Oechsner, Behavior of DLC coated low-alloy steel under tribological and corrosive load: Effect of top layer and interlayer variation, Surf. Coat. Technol. 215 (2013) 110–118, https://doi.org/10.1016/j.surfcoat.2012.08.075.
[32] L. Li, P. Guo, L.-L. Liu, X. Li, P. Ke, A. Wang, Structural design of Cr/GLC films for high tribological performance in artificial seawater: Cr/GLC ratio and multilayer structure, J. Mater. Sci. Technol. 34 (2018) 1273–1280, https://doi.org/10.1016/j.jmst.2017.12.002.
[33] M. Cui, J. Pu, J. Liang, L. Wang, G. Zhang, Q. Xue, Corrosion and tribocorrosion performance of multilayer diamond-like carbon film in NaCl solution, RSC Adv. 5 (2015) 104829–104840, https://doi.org/10.1039/c5ra21207c.
[34] U. Depner, J. Ellermeier, T. Trossmann, C. Berger, M. Oechsner, The effect of layer structure on corrosion and erosion resistance of thin PVD multilayer films, Int. J. Mater. Res. 102 (2011) 1014–1020, https://doi.org/10.3139/146.110548.
[35] P. Panjan, D. Kek Merl, F. Zupanič, M. Čekada, M. Panjan, SEM study of defects in PVD hard coatings using focused ion beam milling, Surf. Coat. Technol. 202 (2008) 2302–2305, https://doi.org/10.1016/j.surfcoat.2007.09.033.
[36] P. Panjan, M. Čekada, M. Panjan, D. Kek-Merl, Growth defects in PVD hard coatings, Vacuum 84 (2009) 209–214, https://doi.org/10.1016/j.vacuum.2009.05.018.
[37] L. Li, L.L. Liu, X. Li, P. Guo, P. Ke, A. Wang, Enhanced tribocorrosion performance of Cr/GLC multilayered films for marine protective application, ACS Appl. Mater. Interfaces 10 (2018) 13187–13198, https://doi.org/10.1021/acsami.8b00628.
[38] Y. Liu, H. Du, X. Zuo, P. Guo, L. Liu, K.-R. Lee, A. Wang, P. Ke, Cr/GLC multilayered coating in simulated deep-sea environment: corrosion behavior and growth defect evolution, Corros. Sci. 188 (2021), https://doi.org/10.1016/j.corsci.2021.109528.
[39] S.J. Park, K.-R. Lee, S.-H. Ahn, J.-G. Kim, Instability of diamond-like carbon (DLC) films during sliding in aqueous environment, Diam. Relat. Mater. 17 (2008) 247–251, https://doi.org/10.1016/j.diamond.2007.12.035.

[40] P. Panjan, A. Drnovšek, P. Gselman, M. Čekada, M. Panjan, Review of growth defects in thin films prepared by PVD techniques, Coatings 10 (2020), https://doi.org/10.3390/coatings10050447.
[41] R.N. Tait, T. Smy, S.K. Dew, M.J. Brett, Nodular defect growth and structure in vapor deposited films, J. Electron. Mater. 24 (1995) 935–940, https://doi.org/10.1007/BF02652964.
[42] P. Panjan, P. Gselman, D. Kek-Merl, M. Cekada, M. Panjan, G. Drazic, T. Boncina, F. Zupanic, Growth defect density in PVD hard coatings prepared by different deposition techniques, Surf. Coat. Technol. 237 (2013) 349–356, https://doi.org/10.1016/j.surfcoat.2013.09.020.
[43] D.M. Mattox, Surface effects on the growth, adhesion and properties of reactively deposited hard coatings, Surf. Coat. Technol. 81 (1996) 8–16, https://doi.org/10.1016/0257-8972(95)02652-5.
[44] S. Zhu, L. Chen, Y. Wu, Y. Hu, T. Liu, K. Tang, Q. Wei, Microstructure and corrosion resistance of Cr/Cr2N multilayer film deposited on the surface of depleted uranium, Corros. Sci. 82 (2014) 420–425, https://doi.org/10.1016/j.corsci.2014.02.011.
[45] D.G. Stearns, P.B. Mirkarimi, E. Spiller, Localized defects in multilayer coatings, Thin Solid Films 446 (2004) 37–49, https://doi.org/10.1016/S0040-6090(03)01285-9.
[46] A. Zeng, E. Liu, I.F. Annergren, S.N. Tan, S. Zhang, P. Hing, J. Gao, EIS capacitance diagnosis of nanoporosity effect on the corrosion protection of DLC films, Diam. Relat. Mater. 11 (2002) 160–168, https://doi.org/10.1016/S0925-9635(01)00568-4.
[47] W. Tian, L. Liu, F. Meng, Y. Liu, Y. Li, F. Wang, The failure behaviour of an epoxy glass flake coating/steel system under marine alternating hydrostatic pressure, Corros. Sci. 86 (2014) 81–92, https://doi.org/10.1016/j.corsci.2014.04.038.
[48] A.M.M. dos Santos, R.J.C. Batista, L.A.M. Martins, M. Ilha, M.Q. Vieira, D. R. Miquita, F.C.R. Guma, I.L. Muller, T.M. Manhabosco, Corrosion and cell viability studies of graphite-like hydrogenated amorphous carbon films deposited on bare and nitrided titanium alloy, Corros. Sci. 82 (2014) 297–303, https://doi.org/10.1016/j.corsci.2014.01.025.
[49] S. Skale, V. Doleček, M. Slemnik, Substitution of the constant phase element by Warburg impedance for protective coatings, Corros. Sci. 49 (2007) 1045–1055, https://doi.org/10.1016/j.corsci.2006.06.027.
[50] S. Rudenja, J. Pan, I. Wallinder, C. Leygraf, P. Kulu, Passivation and anodic oxidation of duplex TiN coating on stainless steel, J. Electrochem. Soc. 146 (1999) 4082–4086, https://doi.org/10.1149/1.1392595.
[51] C. Liu, Q. Bi, A. Leyland, A. Matthews, An electrochemical impedance spectroscopy study of the corrosion behaviour of PVD coated steels in 0.5 N NaCl aqueous solution: Part II.: EIS interpretation of corrosion behaviour, Corros. Sci. 45 (2003) 1257–1273, https://doi.org/10.1016/S0010-938X(02)00214-7.
[52] R. Vedalakshmi, V. Saraswathy, H.-W. Song, N. Palaniswamy, Determination of diffusion coefficient of chloride in concrete using Warburg diffusion coefficient, Corros. Sci. 51 (2009) 1299–1307, https://doi.org/10.1016/j.corsci.2009.03.017.
[53] X. Li, Y. Jiang, Z. Jiang, Y. Li, C. Wen, D. Zhang, J. Lian, Z. Zhang, Improvement of corrosion resistance of H59 brass through fabricating superhydrophobic surface using laser ablation and heating treatment, Corros. Sci. 180 (2021), https://doi.org/10.1016/j.corsci.2020.109186.
[54] M. Stern, A.L. Geaby, Electrochemical polarization, J. Electrochem. Soc. 104 (1957) 56, https://doi.org/10.1149/1.2428496.
[55] H.J. Flitt, D.P. Schweinsberg, Evaluation of corrosion rate from polarisation curves not exhibiting a Tafel region, Corros. Sci. 47 (2005) 3034–3052, https://doi.org/10.1016/j.corsci.2005.06.014.
[56] Y.L. Chipatecua, J.J. Olaya, D.F. Arias, Corrosion behaviour of CrN/Cr multilayers on stainless steel deposited by unbalanced magnetron sputtering, Vacuum 86 (2012) 1393–1401, https://doi.org/10.1016/j.vacuum.2012.01.016.
[57] A. Ruden, E. Restrepo-Parra, A.U. Paladines, F. Sequeda, Corrosion resistance of CrN thin films produced by dc magnetron sputtering, Appl. Surf. Sci. 270 (2013) 150–156, https://doi.org/10.1016/j.apsusc.2012.12.148.
[58] G.-H. Song, X.-P. Yang, G.-L. Xiong, Z. Lou, L.-J. Chen, The corrosive behavior of Cr/CrN multilayer coatings with different modulation periods, Vacuum 89 (2013) 136–141, https://doi.org/10.1016/j.vacuum.2012.02.046.